Autocatalytic reduction-assisted synthesis of segmented porous PtTe nanochains for enhancing methanol oxidation reaction

Qiqi Zhang[1,2], Tianyu Xia[3] (✉), He Huang[4], Jialong Liu[5] (✉), Mengyuan Zhu[4], Hao Yu[4], Weifeng Xu[4], Yuping Huo[1,2], Congli He[1], Shipeng Shen[1], Cong Lu[6], Rongming Wang[7], and Shouguo Wang[1,4,7,8] (✉)

[1] Institute of Advanced Materials, Beijing Normal University, Beijing 100875, China

[2] College of Nuclear Science and Technology, Beijing Normal University, Beijing 100875, China

[3] Key Laboratory of Materials Physics of the Ministry of Education, School of Physics and Microelectronics, Zhengzhou University, Zhengzhou 450052, China

[4] Beijing Advanced Innovation Center for Materials Genome Engineering, School of Materials Science and Engineering, University of Science and Technology Beijing, Beijing 100083, China

[5] Department of Physics and Electronics, School of Mathematics and Physics, Beijing University of Chemical Technology, Beijing 100029, China

[6] Synchrotron Radiation Research Center, Hyogo Science and Technology Association, Tatsuno 6795165, Japan

[7] Institute for Multidisciplinary Innovation, University of Science and Technology Beijing, Beijing 100083, China

[8] School of Materials Science and Engineering, Anhui University, Hefei 230601, China

ABSTRACT

Morphology engineering has been developed as one of the most widely used strategies for improving the performance of electrocatalysts. However, the harsh reaction conditions and cumbersome reaction steps during the nanomaterials synthesis still limit their industrial applications. Herein, one-dimensional (1D) novel-segmented PtTe porous nanochains (PNCs) were successfully synthesized by the template methods assisted by Pt autocatalytic reduction. The PtTe PNCs consist of consecutive mesoporous architectures that provide a large electrochemical surface area (ECSA) and abundant active sites to enhance methanol oxidation reaction (MOR). Furthermore, 1D nanostructure as a robust sustaining frame can maintain a high mass/charge transfer rate in a long-term durability test. After 2,000 cyclic voltammetry (CV) cycles, the ECSA value of PtTe PNCs remained as high as 44.47 $m^2 \cdot g_{Pt}^{-1}$, which was much larger than that of commercial Pt/C (3.95 $m^2 \cdot g_{Pt}^{-1}$). The high catalytic activity and durability of PtTe PNCs are also supported by CO stripping test and density functional theory calculation. This autocatalytic reduction-assisted synthesis provides new insights for designing efficient low-dimensional nanocatalysts.

KEYWORDS

autocatalytic process, PtTe catalysts, methanol oxidation reactions, porous nanochain

1 Introduction

Direct methanol fuel cells (DMFCs) have attracted extensive attention due to their pollution-free, scalability, sustainability, and convenience of transportation [1]. Pt is an ideal anode catalyst because of its distinct electronic properties for methanol oxidation reaction (MOR) in DMFCs [2]. However, several critical issues of Pt catalysts enormously limit the performance of DMFCs in large-scale commercialization, such as high cost, easily poisoned by the intermediates, and poor durability [3–6]. Introducing transition metals or oxide nanoparticles into Pt-based nanostructures to modify the energy band structure through strain or ligand effects provides an effective way to improve the catalytic behavior [7–9]. However, preparing

Pt-based catalysts using simple and efficient strategies for commercial demands remain a challenge. Numerous strategies to enhance the performance of Pt-based electrocatalysts have been reported, including crystal defect building, material ingredient changing, morphology engineering, and so on [10–13].

Recently, morphology engineering has been demonstrated as one of the accessible ways to meet high-quality catalysts [14–18]. Among various architectures, open nanostructures are of great importance due to their large surface-to-volume ratio, abundant surface defects, considerable conductivity, and low Pt consumption, which endows outstanding catalytic behavior in MOR [19–21]. However, some drawbacks still exist, such as random stacking on the electrode, reducing the transmission

Address correspondence to Tianyu Xia, tyxia@zzu.edu.cn; Jialong Liu, Jialongliu@buct.edu.cn; Shouguo Wang, sgwang@bnu.edu.cn

and diffusion of the ions and electrons, lowering structural stability due to the hollow nanostructure, and further limiting the long-term electrochemical performance [13, 22]. In contrast, one-dimensional (1D) nanocatalysts compensate for these deficiencies because of their robust architecture, strong shape anisotropy, higher flexibility, and efficient conductivity [23, 24]. However, the flat and smooth surface cannot offer enough active sites for the reaction, restraining their catalytic activity. Hence, 1D Pt-based porous nanostructures, combining the morphology advantages of patulous and 1D nanostructures, are promoted as reasonable candidates for superior electrocatalysts. Additionally, the segmented construction can further extend the structural benefits to establish more active sites and promote catalytic performance.

Moreover, the tedious steps and harsh reaction conditions strictly limit large-scale manufacturing in commercial applications. It is essential to explore a simple strategy to efficiently fabricate 1D Pt-based porous catalysts with high electrochemical performance. The autocatalytic process has been used to synthesize porous and branched nanostructures, particularly in the reduction of Pt^{2+} or Pt^{4+} precursors, which is a spontaneous reaction occurring under suitable conditions [25, 26]. This reaction can not only affect the interfacial energy, thus, modify the growth environment in the following reactions, but also save avoidable reductants during the synthesis. The growth of Pt-based materials with specific morphologies using an autocatalytic process can simplify the reaction process and improve the catalytic efficiency of the products [27, 28].

Here, 1D PtTe porous nanochains (PNCs) were successfully synthesized with the assistance of the autocatalytic reduction process at room temperature. The Te nanowires (NWs) and Pluronic F127 are served as self-sacrificial and soft templates to maintain the linear shape and mesoporous structures, respectively. Furthermore, Pt autocatalytic reduction mainly determines the formation of protruding structures on the PtTe NWs. The exotic 1D PtTe PNCs possess large specific surface area, abundant defects, fast mass/charge transport rate, and bimetallic alloy synergistic function, jointly leading to enhanced catalytic activity and durability during the MOR process. Finally, the CO stripping test along with the density functional theory (DFT) calculations indicate the high CO adsorption capacity of PtTe PNCs.

2 Experimental details

2.1 Materials and chemicals

Na_2TeO_3 (99.9%) and $N_2H_4 \cdot H_2O$ (80%) were purchased from Aladdin Industrial (Shanghai, China) and Xilong Scientific (Guangdong, China), respectively. $NH_3 \cdot H_2O$ (8 wt.%), poly(vinylpyrrolidone) (PVP, K-30, AR), and ascorbic acid (AA, 99.7%) were bought from Macklin (Shanghai, China). Pluronic F127, K_2PtCl_6, and Nafion solution (5 wt.%) were purchased from Sigma-Aldrich. Commercial Pt/C (40 wt.% Pt) catalyst was purchased from Alfa Aesar. All reagents were of analytic grade and were used as received.

2.2 Synthesis of Te NWs

First, 92 mg Na_2TeO_3 and 1 g PVP were dissolved in 35 mL deionized water and stirred vigorously, then, 3.35 mL $NH_3 \cdot H_2O$ and 1.75 mL $N_2H_4 \cdot H_2O$ were added to the mixed solution. The resultant solution was heated to 180 °C and maintained for 3 h in a 50 mL Teflon-lined stainless-steel autoclave. The solution

was then cooled to room temperature, yielding dark-blue products, and stored in a sealed environment. Finally, 0.75 mL of the obtained solution was dispersed in 1.25 mL acetone and 2 mL deionized water, then the Te NWs (precipitate) were cleaned several times with water and centrifuged under 12,000 rpm. Finally, the product was dissolved in 1 mL deionized water for further use.

2.3 Synthesis of PtTe PNCs

Firstly, 20 mg F127 was completely dissolved in 6.5 mL K_2PtCl_6 (5 mM) water solution, then 0.3 mL Te NWs was added to the solution in an ultrasonic bath. Five minutes later, 3 mL AA (0.1 M) was added, and the homogeneous solution was sonicated for 2 h. Finally, the obtained PtTe PNCs were washed severally with water, precipitated by centrifugation at 5,000 rpm for five min and dispersed in the alcohol solution. PtTe mesoporous nanotubes (MNTs) were successfully obtained when 0.3 mL Te NWs and 3 mL AA were simultaneously added to the mixture under the same experimental conditions.

2.4 Structural characterization

The morphology, microstructure, and composition of the as-synthesized samples were characterized by scanning electron microscopy (SEM, Hitachi S-4800, Hitachi, Tokyo, Japan), transmission electron microscopy (TEM, JEM-2200FS, JEOL, Tokyo, Japan), energy dispersive spectroscopy (EDS, X-Max80T, Oxford Instruments), spherical aberration-corrected transmission electron microscopy (JEM-ARM200F NEOARM, JEOL, Tokyo, Japan), and inductively coupled plasma mass spectrometry (ICP-MS, Thermo Scientific, USA). The crystal and elemental electronic structure analysis were conducted by X-ray diffraction (XRD, Ultima IV, Rigaku, Tokyo, Japan) and X-ray photoelectron spectroscopy (XPS, ESCALAB 250Xi, Thermo VG Scientific, West Sussex, England), respectively.

2.5 Electrochemical characterization

The electrochemical properties of the samples for the MOR process were determined using a CH Instruments 660D electrochemical workstation at room temperature. A typical 3-electrode system consists of a glass carbon disk (0.071 cm²), Pt wire, and a saturated calomel electrode as the working, the counter, and the reference electrodes, respectively. The glass electrode was successively polished with 0.3 and 0.05 μm alumina powder to obtain a mirror-finish surface and cleaned under sonication with ethanol for further testing before the measurements. Then, 2 mg PtTe PNCs was dissolved in 10 mL ethanol and the solution was ultra-sonicated for 20 min. After that, 10 μL of the resultant suspension was dropped onto the surface of the working electrode. Finally, the electrode was air-dried and coated with 5 μL of 5 wt.% Nafion membrane. The samples with PtTe MNTs and commercial Pt/C (40 wt.% Pt) were prepared following the same process outlined for PtTe PNCs, with the same Pt quality obtained.

2.6 First-principles calculation

First-principles calculation in this work was conducted by the DFT implemented in the Vienna *Ab initio* simulation package using the generalized gradient approximation with the Perdew–Burke–Ernzerhof functional [29–31]. Then, a 4 × 4 Pt (111) and PtTe (111) slabs with Te substituting Pt on the top layer were constructed. Different adsorption configurations of CO on Pt and PtTe slabs were enumerated to obtain the most

stable sites. The cutoff energy was set to 520 eV and a 3 × 3 × 1 Monkhorst–Pack k-point mesh was sampled. The vacuum layers were set larger than 15 Å to avoid periodic boundary condition interaction [32]. The DFT-D3 method was adopted to consider the van der Waals interaction for CO adsorption/desorption [33]. All structures were fully relaxed until the total energy, and residual force convergence reached 10^{-5} eV and 0.02 eV·Å^{-1}, respectively. The Gibbs free energy change (ΔG) of CO adsorption on the Pt and PtTe slabs were calculated according to the following:

$$\Delta G = G_{CO+sub} - G_{sub} - G_{CO} \qquad (1)$$

where G_{CO+sub} and G_{sub} represent the Gibbs free energies of the slabs with and without the adsorbed CO. G_{CO} represents the Gibbs free energy of the CO molecule. Especially, the corresponding Gibbs free energy was evaluated by considering the zero-point energy and vibrational entropy effect, which is defined as follows:

$$\Delta G = E + E_{zpe} - T\Delta S \qquad (2)$$

where E_{zpe} and $T\Delta S$ represent the zero-point and vibrational entropy energies of adsorbed CO. Temperature was set to 298.15 K. All these energy corrections were conducted using the Vaspkit package [34].

3 Results and discussion

The morphology and microstructure of the as-prepared PtTe PNCs were first characterized by SEM and TEM. Figures 1(a), 1(b), and Figs. S1(a)–S1(d) in the Electronic Supplementary Material (ESM) show the SEM images of PtTe PNCs, indicating that the dominant products are segmented 1D porous nanochains enclosed by continuously mesoporous structures. The entire length is approximately hundreds of nanometers, where the diameter of these pellets is around 80 nm. Many uniform mesoporous with a size of around 12 nm can be observed on each spherical structure, which may greatly increase the contact area between the catalysts and the acid electrolytes, thus, improving catalytic performance. The atomic percentages of Pt and Te is determined to be 95% and 5% by ICP-MS. Figures 1(c)–1(e) present the typical TEM images at different magnifications, which are used to highlight the detailed structure of the obtained PtTe PNCs. As shown in Fig. 1(c), the 1D PtTe PNCs consist of multiple nanospheres with uneven surfaces, in good agreement with the SEM results. The SAED pattern of PtTe PNCs is shown in the inset of Fig. 1(c), which can be calibrated into (111), (200), (220), and (311) facets of the face-centered cubic (*fcc*) crystal structure, also indicating the high crystallinity of PtTe PNCs [35]. The high-resolution TEM (HRTEM) images shown in Figs. 1(d) and 1(e) confirm that the porous spheres were composed of many small nanoparticles with an average size of 3 nm, and these nanoparticles have numerous low index facets, steps, and corner atoms (Figs. S2(a)–S2(c) in the ESM). The lattice spacing of 0.22 nm was calculated from Fig. 1(e), corresponding to the (111) as a typical *fcc* crystal structure for Pt. The high angle annular dark-field scanning TEM (HAADF–STEM) and elemental Pt and Te mapping of a single 1D PtTe PNC (Fig. 1(f)) reveal that Pt is homogeneously distributed throughout the nanochain, while the distribution of Te is relatively concentrated in the central part. These special porous structures, numerous steps corner atoms, and efficient Pt-rich surface are greatly favorable for electrocatalytic applications. The crystal structure
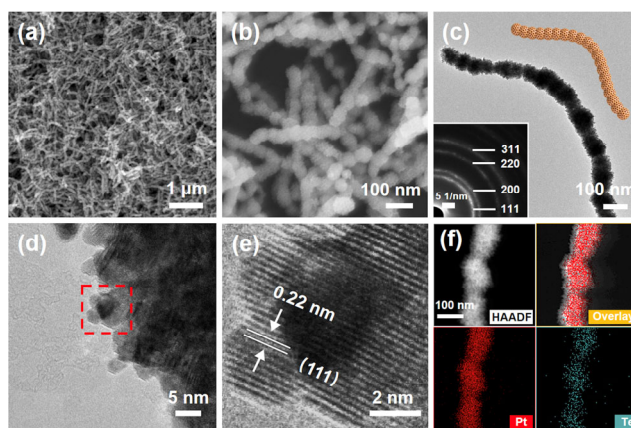

Figure 1 Structural characterization of PtTe PNCs. (a, b) SEM and (c, d) TEM images. Insets are the selected area electron diffraction (SAED) pattern. (e) HRTEM image for the square area. (f) HAADF–STEM image and their corresponding EDS mapping profiles for Pt (red) and Te (blue).
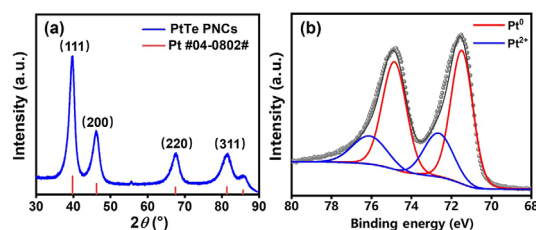

Figure 2 (a) XRD pattern for PtTe PNCs. (b) XPS spectra of Pt 4f with two peaks from metallic Pt^0 and oxidized Pt^{2+} for PtTe PNCs.

of PtTe PNCs was also determined by XRD (Fig. 2(a)), where three distinct diffraction peaks at 39.90°, 46.27°, and 67.77° can be indexed to the (111), (200), and (220) facets of *fcc* crystal structure of Pt, respectively, in good agreement with the SAED pattern. Compared to the Pt standard peaks (PDF #04-0802), the diffraction peaks of PtTe PNCs are slightly shifted without any single Te diffraction peaks, indicating the PtTe-alloyed nanostructure. The XPS measurements were conducted to analyze the surface composition and electronic properties of PtTe PNCs, as shown in Fig. 2(b). The Pt 4f peaks can be divided into two pairs, including metallic Pt^0 and oxidized Pt^{2+}, and the majority state of PtTe PNCs is Pt^0, which primarily contributes to enhancing the electrocatalytic activity during MOR. Pt 4f$_{5/2}$ and Pt 4f$_{7/2}$ peaks for Pt^0 are located at 74.9 and 71.5 eV, respectively. These two peaks marginally deviate from the standard peaks at 74.25 and 70.9 eV for Pt 4f$_{5/2}$ and 4f$_{7/2}$, respectively [36], indicating that Te may lower the d-band center of Pt, which could be a crucial factor in enhancing the electrocatalytic performance of the PtTe alloy [37]. The XRD and XPS for Pt/C and Te NWs are provided in Figs. S3 and S4 in the ESM.

To gain more insight into the morphological evolution of PtTe PNCs, the morphologies at different growth stages were observed by SEM and TEM (Fig. S5 in the ESM), and the process is illustrated in Fig. 3. As shown in Fig. 3(a) and Fig. S5(a) in the ESM, the Te NWs with an average diameter of around 7 nm act as self-sacrificial templates to maintain the linear structure of the samples. At the initial stage of the reaction (Fig. 3(b) and Fig. S5(b) in the ESM), PtCl$_6^{2-}$ ions were reduced on the Te NWs surface to form PtTe NWs according to the galvanic replacement reaction [38]:

$$[PtCl_6]^{2-} + Te + 3H_2O \rightarrow Pt + TeO_3^{2-} + 6Cl^- + 6H^+ \qquad (3)$$
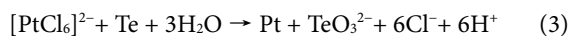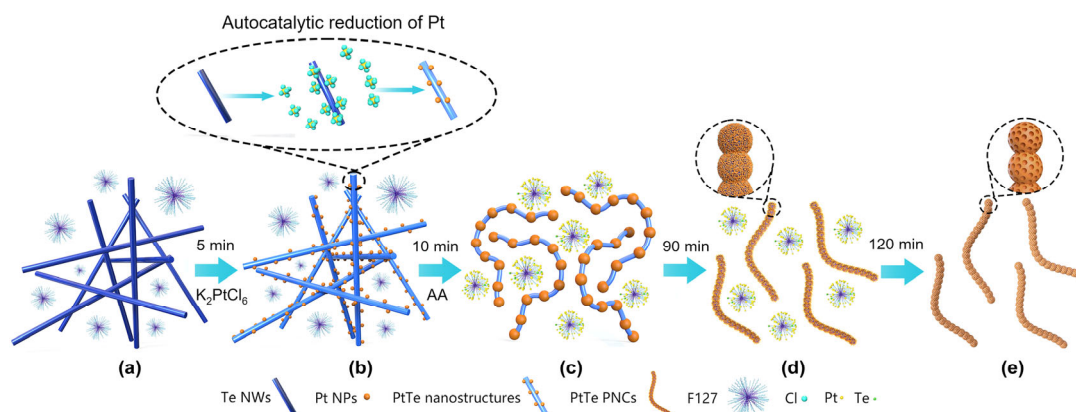
Figure 3 Schematic of the synthesis of the PtTe PNCs.

Once Pt atoms are formed on the surface of PtTe NWs, the autocatalytic process will be triggered in a highly concentrated solution of $PtCl_6^{2-}$ ions. As the reaction proceeds, more zero-valent Pt atoms are auto-catalytically reduced out from $PtCl_6^{2-}$ ions at an ultrahigh reaction rate and stacked on the surface of PtTe NWs as new autocatalytic reaction sites and assembled locations [25, 39]. The composition of these PtTe NWs decorated by Pt nanoparticles are identified as $Pt_{75}Te_{25}$ from the analysis of EDS (as shown in Fig. 2(b)). After the AA is added, the precursors are slowly reduced and continue to accumulate on the surface, which raised the sites of the 1D nanostructures (Figs. 3(c), 3(d) and Figs. S5(c)–S5(f) in the ESM). The uniform segmented 1D porous nanostructures are well formed after 120 min, as shown in Fig. 3(e). Whether the autocatalytic reaction of Pt can proceed smoothly and even eventually form chain-like nanostructures was directly determined by the additional time of AA and the concentration of Pt precursors. As previously reported [40], if AA and Te NWs were added simultaneously, the products named PtTe MNTs would be assembled without surface undulation (Fig. S6 in the ESM). Alternatively, when the amount of Pt precursors is decreased to 10 or 20 mmol, only incomplete 1D nanostructures can be formed (Figs. S7(a) and S7(b) in the ESM) due to the lack of enough quantities of Pt atoms to participate in the formation of porous structures. Conversely, when the concentration of Pt precursors is increased to 40 mmol, as shown in Fig. S7(c) in the ESM, a large excess of Pt atoms is stacked on the surface of the 1D structural bulge by thermodynamic factors, resulting in a nonuniform growth of the bulge. The dose of Te NWs as sacrificial templates were also similarly studied, and irregular shapes can be observed in Figs. S7(d)–S7(f) in the ESM. Additionlly, the porous nanostructures are attributed to the joint effect of F127 and AA. During the reaction, Pt_mCl_n complex formed by the precursors combined with water molecules was easily adsorbed on the ethylene oxide chain of F127 [41]. Since the ethylene oxide chain is an evanescent chain structure, the Pt_mCl_n adsorbed on its terminals can still maintain the initial structure after being reduced by AA, and finally, form a 1D porous nanostructure [42].

When F127 is replaced by other surfactants (such as PVP shown in Fig. S8(a) in the ESM), nonporous structures can be observed in the as-prepared products. Once the strong reductant $NaBH_4$ is added in this system instead of AA, the final products will consist of two components (NWs and nanospheres) because the $PtCl_6^{2-}$ ions are directly reduced to form the Pt nanospheres (Figs. S8(b) and S8(c) in the ESM).
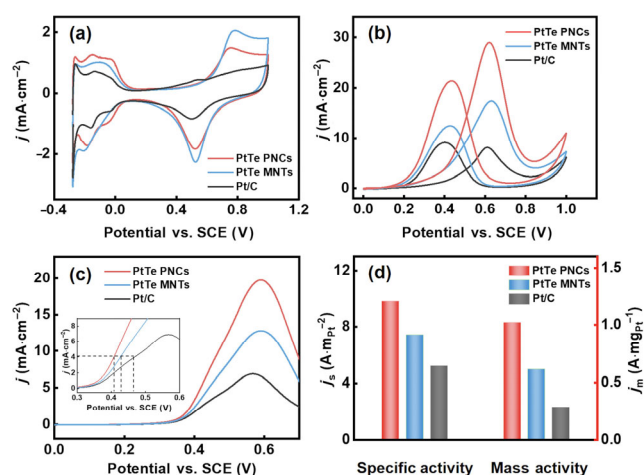

Figure 4 CV curves of PtTe PNCs, PtTe MNTs, and commercial Pt/C in (a) 0.5 M H_2SO_4 and (b) a mixed solution of 0.5 M H_2SO_4 and 1 M CH_3OH. (c) LSV of the three catalysts in a mixed solution of 0.5 M H_2SO_4 and 1 M CH_3OH. Inset of (c): amplification of LSV curves between 0.3–0.6 V. (d) Specific and mass activities of PtTe PNCs, PtTe MNTs, and commercial Pt/C, respectively.

Additionally, the amount of F127 also dominates the pore size of the porous nanostructures, and when the amount of F127 is increased, the pore diameter gradually decreases, leading to a denser porous structure (Figs. S8(d) and S8(e) in the ESM). As for the catalytic performance, the PtTe PNCs, PtTe MNTs, and commercial Pt/C (40 wt.% Pt) catalysts were investigated under the same test conditions. The electrochemically active surface area (ECSA) was calculated from the CV curves in N_2-saturated 0.5 M H_2SO_4 at a scan rate of 50 $mV \cdot s^{-1}$, as shown in Fig. 4(a). The ECSA value is determined to be 104.34, 82.80, and 54.95 $m^2 \cdot g_{Pt}^{-1}$ for PtTe PNCs, PtTe MNTs, and commercial Pt/C, respectively. The high ECSA value for PtTe PNCs can mainly be attributed to their uniform 1D porous nanostructure, small-sized Pt nanoparticles, and more index facets, which will be discussed in detail later. The CV curves were also acquired to evaluate the electrocatalytic properties in 0.5 M H_2SO_4 and 1 M CH_3OH mixed solution at a scan rate of 50 $mV \cdot s^{-1}$. Two typical prominent peaks located at 0.42 and 0.62 V can be observed in the forward and backward scanning curves, respectively (Fig. 4(b)). The forward current density (j_i) of PtTe PNCs (28.94 $mA \cdot cm^{-2}$) was brightly larger than that of PtTe MNTs (17.41 $mA \cdot cm^{-2}$) and commercial Pt/C (8.14 $mA \cdot cm^{-2}$), indicating the higher activity of PtTe PNCs. Linear sweep

voltammetry (LSV) curves were obtained at a slow scan rate (5 mV·s⁻¹) in a mixed solution containing 0.5 M H₂SO₄ and 1 M CH₃OH (Fig. 4(c)). For a given oxidation current density, such as the baseline of 4 mA·cm⁻² shown in the inset of Fig. 4(c), the corresponding oxidation potential of PtTe PNCs (0.41 V) is lower than that of PtTe MNTs (0.43 V) and commercial Pt/C (0.47 V), indicating that a faster methanol-oxidized process occurs on the surface of PtTe PNCs and it can deliver high quality current to the device at a lower voltage. Figure 4(d) shows the specific and mass activities of the three catalysts calculated from the values of ECSA and Pt loading mass normalization of the forward peak current density. The PtTe PNCs exhibit a superior specific activity (9.80 A·m$_{Pt}^{-2}$), resulting in 1.3- and 1.8-fold improvements over PtTe MNTs (7.43 A·m$_{Pt}^{-2}$) and commercial Pt/C (5.23 A·m$_{Pt}^{-2}$), respectively. The mass activity of PtTe PNCs was 1.02 A·mg$_{Pt}^{-1}$, leading to 1.6- and 3.5-fold improvements over PtTe MNTs (0.62 A·mg$_{Pt}^{-1}$) and commercial Pt/C (0.29 A·mg$_{Pt}^{-1}$), respectively. The good electrochemical performance of PtTe PNCs greatly depends on the special segmented PtTe porous nanochains, some active facets, and modification of the surface electronic environment between the Te and Pt atoms.

The electrocatalytic durability of the three catalysts was measured via chronoamperometry in 0.5 M H₂SO₄ and 1 M CH₃OH mixed solution at a fixed potential of 0.6 V (Fig. 5(a)). The continuous currents show a rapid drop with respect to time for the three catalysts due to the poisoning species and intermediates accumulating on the catalyst surface, which induces a decrease in active sites [43]. After 1,000 s, the oxidation current density of PtTe PNCs is still much larger than that of PtTe MNTs and commercial Pt/C.

The accelerated durability test was also acquired to evaluate the durability of the three catalysts based on the CV curves in 0.5 M H₂SO₄ and 1 M CH₃OH mixed solution at a scan rate of 50 mV·s⁻¹. The CV curves before and after 2,000 cycles are shown in Figs. S9(a)–S9(f) in the ESM. After 2,000 cycles, the ECSA value of PtTe PNCs was 44.47 m²·g$_{Pt}^{-1}$, which was considerably larger than that of PtTe MNTs (18.34 m²·g$_{Pt}^{-1}$) and commercial Pt/C (3.95 m²·g$_{Pt}^{-1}$), as shown in Fig. 5(c). It can be seen from Fig. 5(d) that the PtTe PNCs still retain 65% of their original mass activity (0.67 A·mg$_{Pt}^{-1}$), whereas it is only

38% and 3% of the original values of PtTe MNTs (0.24 A·mg$_{Pt}^{-1}$) and commercial Pt/C (0.01 A·mg$_{Pt}^{-1}$), respectively. The activity decrease can be primarily attributed to the dissolution of Pt atoms on the surface and the accumulation of some Pt nanoparticles during the catalytic oxidation [44]. The microstructure of PtTe PNCs after 2,000 cycles was examined by TEM (Fig. 5(b) and Figs. S10(a) and S10(b) in the ESM). Notably, the PtTe PNCs still maintain a stable and linear nanostructure due to the robust porous structure and that only the edges are slightly ablated, which supports the above viewpoint. Additionally, the overall well-maintained PtTe PNCs nanostructure is essentially responsible for its excellent durability. Furthermore, the EDS analysis for the PtTe PNCs before and after 2,000 cycles was determined, where the composition of Te changed from 5% to 0.2% due to the gradual precipitation of Te atoms during the MOR (Figs. S11(a)–S11(f) in the ESM) [45].

To better illustrate the resistance of the electrocatalysts to poisoning, the adsorption/desorption capacity of PtTe PNCs for CO was tested and further demonstrated using DFT calculations. As shown in Fig. 6(a), the DFT calculation shows that both pristine Pt (111) and PtTe (111) slabs possess negative CO adsorption energies, indicating the thermodynamic adsorption capacity of CO. However, when Te substitution is introduced, the change of Gibbs free energy (ΔG) for CO adsorption becomes higher, leading to higher efficient CO-removing capacity and better resistance of the electrocatalyst surface to CO poisoning. This result also demonstrates that in PtTe slab, the Pt 3d transitional metal has a more negative d-orbital band center as well as a more electron occupation at the splitting anti-bonding orbitals near the Fermi level, as shown in Fig. 6(b). Meanwhile, the CO stripping curves were collected by the three-electrodes cell on CO monolayer in 0.5 M H₂SO₄ at a scan rate of 50 mV·s⁻¹ (Fig. 6(c)). The CO oxidation peak of PtTe PNCs is located at 0.59 V, which is lower than PtTe MNTs (0.61 V) and commercial Pt/C (0.71 V), indicating that the highly efficient CO removes the capacity of PtTe PNCs, in good agreement with the conclusion drawn from the above first-principles calculation.

Based on the above discussion, it is reasonable to conclude that the enhanced electrocatalytic performance of PtTe PNCs depends on the following three aspects. (i) The 1D PtTe PNCs are constructed from the special segmented porous nanostructure, which not only possess robust structural durability but also exhibit high electronic conductivity and rapid electron/mass transport ability [46]. Furthermore, small-sized nanoparticles with numerous active (111) facets are also significant factors for this outstanding activity. (ii) The autocatalytic process of Pt can effectively reduce the dosage of organic reagents, such as structure-directing agents and reducing agents, greatly streamline the reaction and finally improve the catalyst efficiency. (iii) The synergistic effect between Te and Pt atoms could modify Pt surface electronic environment, thus lowering the d-band center of Pt atoms and allowing more electrons to occupy split anti-bonding orbitals near the Fermi energy level, and subsequently enhancing the activity during MOR.

4 Conclusions

In summary, uniformly segmented PtTe PNCs have been successfully synthesized using a template method along with Pt autocatalytic reduction. The key to this morphology is greatly related to the autocatalytic surface-growth mechanism, which provides the growth site to tune the whole nanostructures.
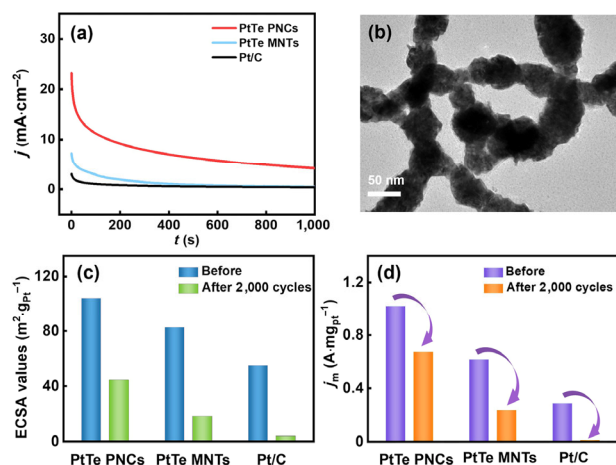

Figure 5 (a) Chronoamperometry curves of the three catalysts obtained in 0.5 M H₂SO₄ and 1 M CH₃OH mixed solution at a fixed potential of 0.6 V, (b) TEM image of PtTe PNCs after 2,000 cycles, (c) ECSA values and (d) mass activities (j_m) of the three catalysts in a mixture of 0.5 M H₂SO₄ and 1 M CH₃OH before and after 2,000 CV cycles.
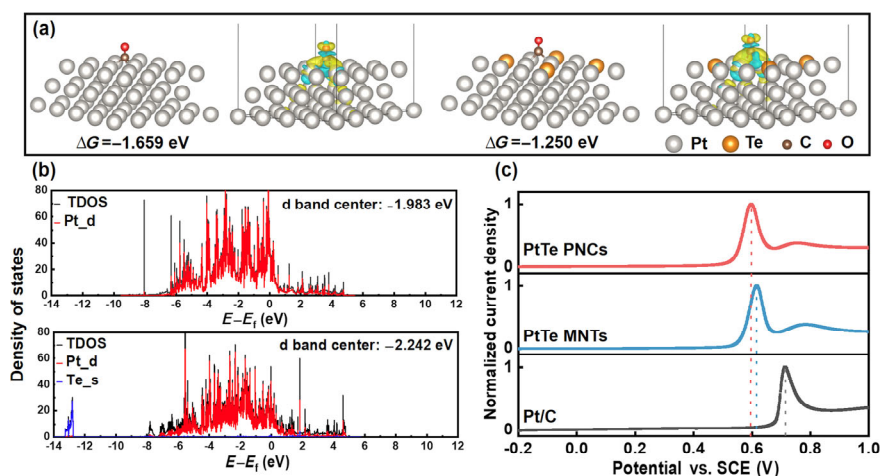
Figure 6 (a) Atomic configuration of CO adsorption on Pt (111) and PtTe (111) slabs and corresponding charge density difference, where the yellow and blue regions indicate electron accumulation and depletion, respectively. The silver, orange, brown, and red balls represent Pt, Te, C, and O atoms, respectively. (b) Partial electronic density of states of Pt (111) and PtTe (111) slabs. The *d*-orbital band centers of Pt are labeled. (c) CO stripping voltammograms of the three catalysts as electrodes in a 0.5 M H_2SO_4 solution at a sweep rate of 50 mV·s^{-1}.

Both Te NWs and F127, which served as self-sacrificial and soft templates, respectively, also play significant roles in maintaining the linear shape and porous structures. The PtTe PNCs exhibit an excellent electrocatalytic performance during MOR, especially with highly efficient CO remove capacity, as demonstrated by CO stripping test and DFT calculations. Such remarkable activity primarily depends on the special structures, which possess the benefits of mass transformation, numerous active facets, and Pt atoms with Te-modified surface structure. This novel porous structure will have considerable potential applications to enhance the electrocatalytic performance and provide a guide for future catalytic research.

Acknowledgements

Electronic Supplementary Material: Supplementary material (additional TEM and SEM images and CV curves) is available in the online version of this article at https://doi.org/10.26599/NRE.2023.9120041.

Declaration of conflicting interests

The authors declare no conflicting interests regarding the content of this article.

References

[1] Verhelst, S.; Turner, J. W. G.; Sileghem, L.; Vancoillie, J. Methanol as a fuel for internal combustion engines. *Prog. Energy Combust. Sci.* **2019**, *70*, 43–88.

[2] Hu, G. F.; Shang, L.; Sheng, T.; Chen, Y. G.; Wang, L. Y. PtCo@NCs with short heteroatom active site distance for enhanced catalytic properties. *Adv. Funct. Mater.* **2020**, *30*, 2002281.

[3] Lou, W. H.; Ali, A.; Shen, P. K. Recent development of Au arched Pt nanomaterials as promising electrocatalysts for methanol oxidation reaction. *Nano Res.* **2022**, *15*, 18–37.

[4] Chen, S.; Huang, D. M.; Liu, D. Y.; Sun, H. Z.; Yan, W. J.; Wang, J. C.; Dong, M.; Tong, X. L.; Fan, W. B. Hollow and porous NiCo$_2$O$_4$ nanospheres for enhanced methanol oxidation reaction and oxygen reduction reaction by oxygen vacancies engineering. *Appl. Catal. B Environ.* **2021**, *291*, 120065.

[5] Bai, G. L.; Liu, C.; Gao, Z.; Lu, B. Y.; Tong, X. L.; Guo, X. Y.; Yang, N. J. Atomic carbon layers supported Pt nanoparticles for minimized CO poisoning and maximized methanol oxidation. *Small* **2019**, *15*, 1902951.

[6] Yang, X. B.; Wang, Q.; Qing, S. J.; Gao, Z.; Tong, X. L.; Yang, N. J. Modulating electronic structure of an Au-nanorod-core-PdPt-alloy-shell catalyst for efficient alcohol electro-oxidation. *Adv. Energy Mater.* **2021**, *11*, 2100812.

[7] Xia, T. Y.; Zhao, K.; Zhu, Y. Q.; Bai, X. Y.; Gao, H.; Wang, Z. Y.; Gong, Y.; Feng, M. L.; Li, S. F.; Zheng, Q. et al. Mixed-dimensional Pt-Ni alloy polyhedral nanochains as bifunctional electrocatalysts for direct methanol fuel cell. *Adv. Mater.*, in press, DOI: 10.1002/adma.202206508.

[8] Lu, S. Q.; Li, H. M.; Sun, J. Y.; Zhuang, Z. B. Promoting the methanol oxidation catalytic activity by introducing surface nickel on platinum nanoparticles. *Nano Res.* **2018**, *11*, 2058–2068.

[9] Cao, Y. Q.; Yang, Y.; Shan, Y. F.; Huang, Z. R. One-pot and facile fabrication of hierarchical branched Pt-Cu nanoparticles as excellent electrocatalysts for direct methanol fuel cells. *ACS Appl. Mater. Interfaces* **2016**, *8*, 5998–6003.

[10] Lu, W. Y.; Xia, X. Y.; Wei, X. X.; Li, M. M.; Zeng, M.; Guo, J.; Cheng, S. Nanoengineering 2D dendritic PdAgPt nanoalloys with edge-enriched active sites for enhanced alcohol electroxidation and electrocatalytic hydrogen evolution. *ACS Appl. Mater. Interfaces* **2020**, *12*, 21569–21578.

[11] Li, Z. J.; Jiang, X.; Wang, X. R.; Hu, J. R.; Liu, Y. Y.; Fu, G. T.; Tang, Y. W. Concave PtCo nanocrosses for methanol oxidation reaction. *Appl. Catal. B Environ.* **2020**, *277*, 119135.

[12] Zhang, Q. Q.; Liu, J. L.; Xia, T. Y.; Qi, J.; Lyu, H. C.; Luo, B. Y.; Wang, R. M.; Guo, Y. Z.; Wang, L. H.; Wang, S. G. Antiferromagnetic element Mn modified PtCo truncated octahedral nanoparticles with enhanced activity and durability for direct methanol fuel cells. *Nano Res.* **2019**, *12*, 2520–2527.

[13] Tian, X. L.; Zhao, X.; Su, Y. Q.; Wang, L. J.; Wang, H. M.; Dang, D.; Chi, B.; Liu, H. F.; Hensen, E. J. M.; Lou, X. W. et al. Engineering bunched Pt-Ni alloy nanocages for efficient oxygen reduction in practical fuel cells. *Science* **2019**, *366*, 850–856.

[14] Yaldagard, M.; Nazoktabar, M.; Jahanshahi, M. Fabrication of platinum/polypyrol-carbon nanofiber nanocomposite electrocatalyst for direct methanol fuel cells. *J. Nano Res.* **2021**, *70*, 101–117.

[15] Pham, H. Q.; Huynh, T. T.; Nguyen, S. T.; Dang, N. N.; Bach, L. G.; Ho, V. T. T. Superior CO-tolerance and stability toward alcohol electro-oxidation reaction of 1D-bimetallic platinum-cobalt nanowires on Tungsten-modified anatase TiO_2 nanostructure. *Fuel* **2020**, *276*, 118078.

[16] Li, M. G.; Zhao, Z. L.; Xia, Z. H.; Yang, Y.; Luo, M. C.; Huang, Y. R.; Sun, Y. J.; Chao, Y. G.; Yang, W. X.; Yang, W. W. et al. Lavender-like Ga-doped Pt_3Co nanowires for highly stable and active electrocatalysis. *ACS Catal.* **2020**, *10*, 3018–3026.

[17] Li, H. Y.; Wu, X. S.; Tao, X. L.; Lu, Y.; Wang, Y. W. Direct synthesis of ultrathin Pt nanowire arrays as catalysts for methanol oxidation. *Small* **2020**, *16*, 2001135.

[18] Liang, M. C.; Xia, T. Y.; Gao, H.; Zhao, K.; Cao, T. Q.; Deng, M.; Ren, X. Y.; Li, S. F.; Guo, H. Z.; Wang, R. M. Modulating reaction pathways of formic acid oxidation for optimized electrocatalytic performance of PtAu/CoNC. *Nano Res.* **2022**, *15*, 1221–1229.

[19] Liang, W. K.; Wang, Y. W.; Zhao, L.; Guo, W.; Li, D.; Qin, W.; Wu, H. H.; Sun, Y. H.; Jiang, L. 3D Anisotropic Au@Pt-Pd hemispherical nanostructures as efficient electrocatalysts for methanol, ethanol, and formic acid oxidation reaction. *Adv. Mater.* **2021**, *33*, 2100713.

[20] Geng, W. C.; Zhang, Y. J.; Yu, L.; Li, J. J.; Sang, J. L.; Li, Y. J. Integrating $Pt_{16}Te$ nanotroughs and nanopillars into a 3D "Self-Supported" hierarchical nanostructure for boosting methanol electrooxidation. *Small* **2021**, *17*, 2101499.

[21] Sha, R.; Jones, S. S.; Badhulika, S. Controlled synthesis of platinum nanoflowers supported on carbon quantum dots as a highly effective catalyst for methanol electro-oxidation. *Surf. Coat. Technol.* **2019**, *360*, 400–408.

[22] Liu, J. L.; Xia, T. Y.; Wang, S. G.; Yang, G.; Dong, B. W.; Wang, C.; Ma, Q. D.; Sun, Y. N.; Wang, R. M. Oriented-assembly of hollow FePt nanochains with tunable catalytic and magnetic properties. *Nanoscale* **2016**, *8*, 11432–11440.

[23] Gao, L.; Yang, Z. L.; Sun, T. L.; Tan, X.; Lai, W. C.; Li, M. F.; Kim, J.; Lu, Y. F.; Choi, S. I.; Zhang, W. H. et al. Autocatalytic surface reduction-assisted synthesis of PtW ultrathin alloy nanowires for highly efficient hydrogen evolution reaction. *Adv. Energy Mater.* **2022**, *12*, 2103943.

[24] Tang, J. X.; Chen, Q. S.; You, L. X.; Liao, H. G.; Sun, S. G.; Zhou, S. G.; Xu, Z. N.; Chen, Y. M.; Guo, G. C. Screw-like PdPt nanowires as highly efficient electrocatalysts for methanol and ethylene glycol oxidation. *J. Mater. Chem. A* **2018**, *6*, 2327–2336.

[25] Ciacchi, L. C.; Pompe, W.; De Vita, A. Growth of platinum clusters via addition of Pt(II) complexes: A first principles investigation. *J. Phys. Chem. B* **2003**, *107*, 1755–1764.

[26] Ciacchi, L. C.; Pompe, W.; De Vita, A. Initial nucleation of platinum clusters after reduction of K_2PtCl_4 in aqueous solution: A first principles study. *J. Am. Chem. Soc.* **2001**, *123*, 7371–7380.

[27] Lim, B.; Lu, X. M.; Jiang, M. J.; Camargo, P. H. C.; Cho, E. C.; Lee, E. P.; Xia, Y. N. Facile synthesis of highly faceted multioctahedral Pt nanocrystals through controlled overgrowth. *Nano Lett.* **2008**, *8*, 4043–4047.

[28] Song, Y. J.; Yang, Y.; Medforth, C. J.; Pereira, E.; Singh, A. K.; Xu, H. F.; Jiang, Y. B.; Brinker, C. J.; Van Swol, F.; Shelnutt, J. A. Controlled synthesis of 2-D and 3-D dendritic platinum nanostructures. *J. Am. Chem. Soc.* **2004**, *126*, 635–645.

[29] Hammer, B.; Hansen, L. B.; Nørskov, J. K. Improved adsorption energetics within density-functional theory using revised Perdew-Burke-Ernzerhof functionals. *Phys. Rev. B* **1999**, *59*, 7413–7421.

[30] Ernzerhof, M.; Scuseria, G. E. Assessment of the Perdew-Burke-Ernzerhof exchange-correlation functional. *J. Chem. Phys.* **1999**, *110*, 5029–5036.

[31] Kresse, G.; Furthmüller, J. Efficient iterative schemes for *ab initio* total-energy calculations using a plane-wave basis set. *Phys. Rev. B* **1996**, *54*, 11169–11186.

[32] Huang, H.; Wu, H. H.; Chi, C.; Huang, B. L.; Zhang, T. Y. *Ab initio* investigations of orthogonal ScC_2 and ScN_2 monolayers as promising anode materials for sodium-ion batteries. *J. Mater. Chem. A* **2019**, *7*, 8897–8904.

[33] Grimme, S.; Antony, J.; Ehrlich, S.; Krieg, H. A consistent and accurate *ab initio* parametrization of density functional dispersion correction (DFT-D) for the 94 elements H-Pu. *J. Chem. Phys.* **2010**, *132*, 154104.

[34] Wang, V.; Xu, N.; Liu, J. C.; Tang, G.; Geng, W. T. VASPKIT: A user-friendly interface facilitating high-throughput computing and analysis using VASP code. *Comput. Phys. Commun.* **2021**, *267*, 108033.

[35] Xia, B. Y.; Wu, H. B.; Li, N.; Yan, Y.; Lou, X. W.; Wang, X. One-pot synthesis of Pt-Co alloy nanowire assemblies with tunable composition and enhanced electrocatalytic properties. *Angew. Chem., Int. Ed.* **2015**, *127*, 3868–3872.

[36] Wagner, C. D.; Riggs, W. M.; Davis, L. E.; Moulder, J. F.; Muilenberg, G. E. *Handbook of X-Ray Photoelectron Spectroscopy*; Physical Electronics Division: Gaithersburg, 1979.

[37] Liu, D. Y.; Zeng, Q.; Hu, C. Q.; Chen, D.; Liu, H.; Han, Y. S.; Xu, L.; Zhang, Q. B.; Yang, J. Light doping of tungsten into copper-platinum nanoalloys for boosting their electrocatalytic performance in methanol oxidation. *Nano Res. Energy* **2022**, *1*, e9120017.

[38] Liang, H. W.; Liu, S.; Gong, J. Y.; Wang, S. B.; Wang, L.; Yu, S. H. Ultrathin Te nanowires: An excellent platform for controlled synthesis of ultrathin platinum and palladium nanowires/nanotubes with very high aspect ratio. *Adv. Mater.* **2009**, *21*, 1850–1854.

[39] Lim, B.; Jiang, M. J.; Camargo, P. H. C.; Cho, E. C.; Tao, J.; Lu, X. M.; Zhu, Y. M.; Xia, Y. N. Pd-Pt bimetallic nanodendrites with high activity for oxygen reduction. *Science* **2009**, *324*, 1302–1305.

[40] Wang, H. J.; Yin, S. L.; Li, C. J.; Deng, K.; Wang, Z. Q.; Xu, Y.; Li, X. N.; Xue, H. R.; Wang, L. Direct synthesis of superlong Pt|Te mesoporous nanotubes for electrocatalytic oxygen reduction. *J. Mater. Chem. A* **2019**, *7*, 1711–1717.

[41] Li, H. H.; Xie, M. L.; Cui, C. H.; He, D.; Gong, M.; Jiang, J.; Zheng, Y. R.; Chen, G.; Lei, Y.; Yu, S. H. Surface charge polarization at the interface: Enhancing the oxygen reduction via precise synthesis of heterogeneous ultrathin Pt/PtTe nanowire. *Chem. Mater.* **2016**, *28*, 8890–8898.

[42] Wang, H. J.; Wang, L.; Sato, T.; Sakamoto, Y.; Tominaka, S.; Miyasaka, K.; Miyamoto, N.; Nemoto, Y.; Terasaki, O.; Yamauchi, Y. Synthesis of mesoporous Pt films with tunable pore sizes from aqueous surfactant solutions. *Chem. Mater.* **2012**, *24*, 1591–1598.

[43] Xiao, L. P.; Li, G.; Yang, Z.; Chen, K.; Zhou, R. S.; Liao, H. G.; Xu, Q. C.; Xu, J. Engineering of amorphous PtO_x interface on Pt/WO_3 nanosheets for ethanol oxidation electrocatalysis. *Adv. Funct. Mater.* **2021**, *31*, 2100982.

[44] Jiang, B.; Li, C. L.; Imura, M.; Tang, J.; Yamauchi, Y. Multimetallic mesoporous spheres through surfactant-directed synthesis. *Adv. Sci.* **2015**, *2*, 1500112.

[45] Li, H. H.; Zhao, S.; Gong, M.; Cui, C. H.; He, D.; Liang, H. W.; Wu, L.; Yu, S. H. Ultrathin PtPdTe nanowires as superior catalysts for methanol electrooxidation. *Angew. Chem., Int. Ed.* **2013**, *52*, 7472–7476.

[46] Pandoli, O. G.; Neto, R. J. G.; Oliveira, N. R.; Fingolo, A. C.; Corrêa, C. C.; Ghavami, K.; Strauss, M.; Santhiago, M. Ultra-highly conductive hollow channels guided by a bamboo bio-template for electric and electrochemical devices. *J. Mater. Chem. A* **2020**, *8*, 4030–4039.
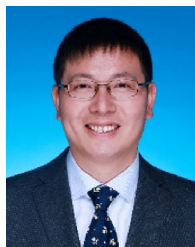
Qiqi Zhang received her master's degree from School of Materials Science and Engineering, University of Science and Technology Beijing in 2020. Currently, she is a Ph.D. student under the supervision by Prof. Shouguo Wang at Beijing Normal University. Her current study focuses on the fabrication and characterization of new energy materials involving electrocatalysts and magnetic materials.

Tianyu Xia received her Ph.D. degree from Department of Physics, Beihang University in 2017. She then joined the Key Laboratory of Materials Physics of the Ministry of Education, School of Physics and Microelectronics, Zhengzhou University. Her current research focuses on the design and application of new energy photo- and electro-catalytic nanomaterials.

Jialong Liu received his Ph.D. degree from Department of Physics, Beihang University in 2016. From July 2016 to May 2021, he worked in the Institute of Geology and Geophysics, Chinese Academy of Sciences. Since May 2021, he joined the School of Mathematics and Physics, Beijing University of Chemical Technology. His research focuses on the synthesis, characterization, and microfabrication of magnetic nanomaterials and their applications in (photo)electrocatalysis.

Shouguo Wang received his bachelor's degree from Anhui University in 1996 and Ph.D. from the Institute of Solid State Physics, Chinese Academy of Sciences (CAS) in 2001, respectively. From August 2001 to December 2007, he carried out research at National University of Singapore, Max-Planck-Institute of Microstructure Physics and University of Oxford. At the end of 2007, he joined the State Key Laboratory of Magnetism, Institute of Physics, CAS. Then he moved to the School of Materials Science and Engineering, University of Science and Technology Beijing in January 2016. He has also worked in Institute of Advanced Materials, Beijing Normal University since 2017. Since July 2022, he has been the Vice President of Anhui University. His research interest includes magnetism and magnetic materials, with a focus on logical magnetism such as skyrmions, spintronics and nanomagnetism.